The formation of satellite droplets by unstable binary drop collisions

G. Brenn
*Lehrstuhl für Strömungsmechanik (LSTM), University of Erlangen-Nürnberg, Cauerstraße 4,
D-91058 Erlangen, Germany*

D. Valkovska and K. D. Danov
*Laboratory of Chemical Physics Engineering, University of Sofia, 1 James Bourchier Avenue,
BG-1164 Sofia, Bulgaria*

Experimental investigations on the process of satellite droplet formation by unstable binary drop collisions are presented. The experiments are carried out using two monodisperse streams of drops of equal size. A systematic variation of the parameters influencing the collisions leads to an extended version of the stability nomogram which involves the numbers of satellite droplets formed by stretching separation after off-center collisions. The time scales for the formation of liquid filaments and their breakup into the satellites are measured and, in the case that a single satellite is formed, the satellite size is measured by means of a phase-Doppler anemometer. Furthermore, a theoretical model for the breakup of cylindrical liquid filaments in head-on and off-center collisions is presented. The model is based on a linear stability analysis of the filament formed after the collision. The critical wavelength associated with the largest deformation energy is calculated and identified with the disturbance which eventually breaks the filament and determines the number of satellites formed. Comparisons with experiments by Ashgriz and Poo [J. Fluid Mech. **221**, 183 (1990)] for the head-on and near-head-on cases yield agreement of the numbers of satellites formed. © *2001 American Institute of Physics.* [DOI: 10.1063/1.1384892]

I. INTRODUCTION

Binary drop collisions are an elementary process in the evolution of dense sprays of droplets in a gaseous environment, which has been the subject of intense research for decades. The collisions may influence the properties of the spray which are important for its application, like average drop size, mass transfer rates, etc., since they may affect the drop size and/or velocity distributions in the spray. This may be the case either due to merging of the colliding droplets (i.e., by stable collisions) or due to the formation of droplets smaller than the colliding drops (i.e., by unstable collisions). In the case of unstable collisions, the breakup of the "complex" drop formed during the impact may take place due to different mechanisms. For head-on or near-head-on collisions, the mechanism was termed "reflexive separation," for off-center collisions we find the term "stretching separation" in the paper by Ashgriz and Poo.[1] Further to these mechanisms, the drops may rebounce after the collision, so that their size remains unaffected. In the present article, this mechanism is not considered.

The stability of the collisions has been a major point of interest in research since the early work by Adam *et al.*[2] Since that time, quite a number of papers on the stability of binary drop collisions has been published, from which different descriptions of the stretching separation of the colliding drops emerged. Since stretching separation is a highly probable process in dense sprays, these results are subsequently discussed in more detail on the basis of the thorough investigation by Ashgriz and Poo.[1]

The first author who reported about experiments on the stretching separation of drops after binary collisions was Park.[3] This author looked at collisions of water droplets in a humid nitrogen environment. He derived an equation for the stability of the drop collisions against stretching separation from balancing the surface forces in the region of contact between the droplets and the forces due to the angular momentum. In the nomenclature of Ashgriz and Poo,[1] which is partly adopted in the present article, Park's equation reads

$$X = \left(\frac{12}{\pi}\right)^{1/2} \frac{(\Delta^2 - \Delta + 1)^{1/2}}{\Delta \, We^{1/2}}$$
$$\times \left[\frac{(1+\Delta^5)(\Delta^2 - \Delta + 1)}{5\Delta^3} + \frac{(1+\Delta)}{2}\right]$$
$$\cdot \left[4 - \left[X(1+\Delta) - \frac{(1-\Delta)}{X}\right]^2\right]^{1/4}, \tag{1}$$

where X is the nondimensional impact parameter $X = 2b/(D_l + D_s)$ (with the large and small drop diameters D_l and D_s and the dimensional impact parameter b as the distance of closest approach of the drop centers measured rectangular to the relative velocity $2U_0$ of the drops), Δ is the ratio of the small and large drop sizes, $\Delta = D_s/D_l$, and We is the Weber number defined as $We = \rho D_s 4 U_0^2/\sigma$, with the density ρ of the drop liquid and the surface tension σ of the drop liquid against the host gas. The equation determines the threshold value of X marking the stability limit for each given We. For values of X above the threshold, stretching separation occurs.

     2463

The next authors to follow in this field of work were Brazier-Smith et al.[4] These authors also carried out experiments on binary water drop collisions and developed a theoretical description of the stability of water drops against stretching separation. The agreement found between experiment and prediction was excellent. The model equation of Brazier-Smith et al.[4] for the stability of the drops against stretching separation is based on the assumption that separation will occur if the rotational energy of the complex drop exceeds the surface energy required to reform the two drops from a coalesced nominal drop. The equation they obtained reads

$$X = \left(\frac{24}{5\text{We}}\right)^{1/2} \frac{(1+\Delta^3)^{11/6}}{(1+\Delta)\Delta^{5/2}} [1+\Delta^2-(1+\Delta^3)^{2/3}]^{1/2}. \quad (2)$$

The physical basis of this equation will be further discussed later in this work. Another approach to a description of the stretching separation instability is due to Arkhipov et al.[5] These authors used the variational principle of minimum potential energy to quantify the stability of the drops against stretching separation by setting the first variation of the potential energy to zero, which was formulated in a coordinate system rotating with constant angular velocity. Arkhipov et al.[5] obtained a relation for the nondimensional impact parameter separating stable coalescence from stretching separation, which reads

$$X = \frac{1}{\Delta^3} \left(\frac{6(1+\Delta^3)}{\text{We}}\right)^{1/2}. \quad (3)$$

Ashgriz and Poo,[1] who provided a thorough discussion of the above three models, developed an alternative model which compared well with their experiments on binary collisions of water drops of the size ratios Δ of 1, 0.75, and 0.5, for the Weber number range of 1 to 100, and for all nondimensional impact parameters X between 0 and 1. The model equation by Ashgriz and Poo[1] reads

$$\text{We} = \frac{4(1+\Delta^3)^2[3(1+\Delta)(1-X)(\Delta^3\phi_s+\phi_l)]^{1/2}}{\Delta^2[(1+\Delta^3)-(1-X^2)(\phi_s+\Delta^3\phi_l)]}, \quad (4)$$

where ϕ_s and ϕ_l are the fractions of the large and small drop volumes which overlap during the collision. They are defined as

$$\phi_s = \begin{cases} 1 - \dfrac{1}{4\Delta^3}(2\Delta-\tau)^2(\Delta+\tau) & \text{for} \quad h > \dfrac{1}{2}D_s, \\[3mm] \dfrac{\tau^2}{4\Delta^3}(3\Delta-\tau) & \text{for} \quad h < \dfrac{1}{2}D_s, \end{cases}$$

$$\phi_l = \begin{cases} 1 - \dfrac{1}{4}(2-\tau)^2(1+\tau) & \text{for} \quad h > \dfrac{1}{2}D_l, \\[3mm] \dfrac{\tau^2}{4}(3-\tau) & \text{for} \quad h < \dfrac{1}{2}D_l, \end{cases}$$

where $\tau \equiv (1-X)(1+\Delta)$, and $h = \frac{1}{2}(D_s+D_l)\cdot(1-X)$, which is the width of the overlapping regions of the colliding

drops. A comparison between the three earlier theoretical models and the new one by Ashgriz and Poo[1] shows that only the models by Ashgriz and Poo[1] and Brazier-Smith et al.[4] adequately predict the stretching separation limit. This comparison is given in Figs. 27–29 of the paper by Ashgriz and Poo.[1] For small drop size ratios of $\Delta=0.5$ and less, Brazier-Smith's model fails to predict the stability limit accurately. Yet, Ashgriz and Poo note that the approach of the earlier models discussed in their paper, to consider angular momentum as the reason for the stretching separation, is not supported by experimental evidence. The experiments show that stretching of the complex drop is due to the inertia of the drops which causes their tendency to move along their initial trajectories. Stretching occurs in the experiments much earlier than any significant rotation can develop. This important result is confirmed by our model of filament instability presented in Sec. IV.

Investigations like the ones discussed earlier were exclusively carried out for water. For practical applications, however, the collisional behavior of drops of liquid fuels like alcohols or n-alkanes is of even bigger importance. It may be due to the large variety of such fuels that investigations like the one by Ashgriz and Poo[1] have not been carried out with fuels in the past. Two thorough surveys of the stability behavior of hydrocarbon drops—which, however, do not provide a mathematical description of the stability limits against stretching separation—are due to Jiang et al.[6] and Qian and Law.[7] These authors presented many details of the stability nomogram of binary drop collisions for $\Delta=1$, where regions of stable coalescence of the droplets, bouncing without mass exchange between the droplets, near-head-on reflexive separation, and stretching separation are identified. Generalized results for the head-on critical Weber numbers We_a (of transition between stable coalescence and bouncing without mass exchange), We_b (of transition between bouncing and stable coalescence at higher Weber numbers), and We_c (of transition between stable coalescence and head-on reflexive separation) are given for different hydrocarbons and water. The results show that these Weber numbers may be represented as a function of the ratio μ/σ of the dynamic liquid viscosity and the surface tension for all liquids under consideration,[6] while the Weber number We_c may be represented as a function of the Ohnesorge number Z of the colliding droplets for a number of hydrocarbons considered.[7]

Another interesting set of experiments on the outcome of binary drop collisions is due to Estrade et al.[8] These authors used a number of alcohols, n-pentane, and water for the investigations and presented stability nomograms, where, to the best knowledge of the present authors, information about the number of satellite droplets formed by unstable binary collisions is included for the first time. The nomograms do not depict boundaries between regions with given numbers of satellites, but the symbols appearing in the nomograms indicate this information. A semi-empirical modeling of reflexive separation after head-on collisions leads to the prediction of the onset Weber number We_c (as denoted by Jiang et al.[6]). The result is an equation for this onset Weber number which agrees with experiments on a wider range of Ohnesorge numbers than the correlation by Jiang et al.[6]

Theoretical work and numerical simulations of binary drop collisions are relatively sparse in the literature. The work by Stone et al.[9] on the deformation and disruption of droplets in well-defined flow fields of a host liquid in a neutrally buoyant system does not (and is not intended to) represent the disintegration of liquid filaments between bulbous ends as they occur in drop collisions in a gaseous environment. Despite these differences, the phenomena of separation of the filament from the bulbous ends and its breakup seem similar to what is observed in collisional drop interaction in a gas. The mechanism of disintegration of the filament is termed ''end pinching.'' A similar liquid–liquid system was treated by the group of Loewenberg and his co-workers,[10,11] who worked on the dynamics of concentrated emulsions and treated the mutual interaction of the dispersed droplets under the influence of the host liquid in shear and buoyancy-driven flow situations. The numerical studies, which used an adaptive marker-tracking method to resolve the strongly deformed drop surfaces, provided all details about the shape of the drops during break-up and sizes of the fragments. Computations by the group around Frohn[12] based on a Lattice–Boltzmann approach also provided valuable and instructive results which represent well the geometrical properties of drop ensembles formed by stretching separation of colliding drops in a gaseous host medium. Despite the unrealistic values of surface tension and viscosity ratio, these computations yield shapes of the complex drop and break-up results very close to experimental observations on drop collisions in air.

Detailed investigations on the disintegration of liquid filaments are due to Stone and his co-workers.[13,14] The biggest part of that work, however, concentrates on liquid–liquid systems, where the dynamic influence of the host medium is far more important than with filaments breaking up in a gaseous environment. We can conclude about the theoretical work that, as yet, no simple model has been developed which could predict at least the number of satellite droplets formed after unstable head-on, near-head-on, or off-center collisions. It is one purpose of the present work to propose such a model, which is verified by comparison with a set of experiments with colliding droplets of propanol-2, and with results from the work by Ashgriz and Poo.[1]

In the following section, we present the apparatus and technique used for our experimental investigation of binary drop collisions. We present a set of results from visualization experiments in Sec. III and then proceed to the description of the model in Sec. IV. Results from the experiments in comparison with the computational results are given in Sec. V. A summary and the conclusions are presented in Sec. VI.

II. EXPERIMENTAL APPARATUS AND TECHNIQUE

In the present section, the test rig used for the drop collision experiments is described. First, the drop generators used for the production of the monodispersed streams of drops are introduced. Then, the measuring equipment—a phase-Doppler anemometer and an image processing system—is described. Finally, the measuring program is presented. The whole test rig is shown in Fig. 1.
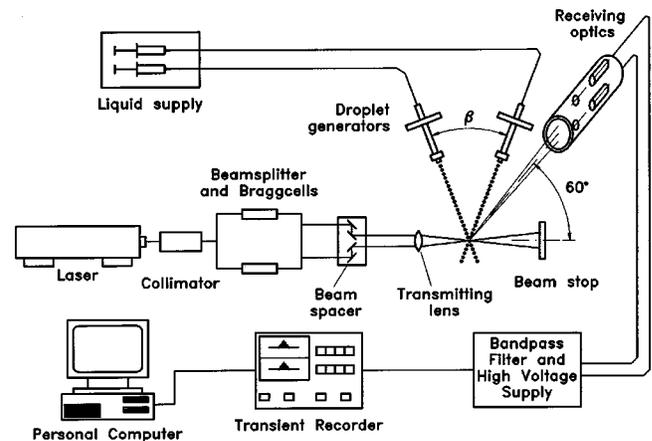

FIG. 1. Sketch of the apparatus used for the experiments.

A. The drop generators

The drop generators used for the experiments consist of a double-walled tube with connections to the liquid supply (upper end), to the nozzle plate holder (lower end), and to the draining hose (see Fig. 2). This latter feature enables flushing of the inner space of the device to ensure that the generator is completely filled with liquid before it is set into operation. The drop generator has relatively small dimensions in the nozzle plane, thus facilitating the relative placement of two such generators for the present investigations. For the production of the drop streams, the liquid was supplied to the drop generators at a constant flow rate from a pressurized liquid reservoir. The syringe pumps sketched in Fig. 1 symbolize the liquid supply. Different flow rates were achieved by varying the driving overpressure of the liquid.

The nozzle plates used in the present experiments were single-hole orifices with a hole diameter $d_h = 30$ μm or $d_h = 50$ μm in stainless steel sheets with 13 μm thickness. The laminar liquid jets emerging from the nozzles are unstable against axisymmetric disturbances and disintegrate into drops. The production of monodisperse drops was forced by exciting the piezoceramic vibrator with an electric DC square-wave signal. This technique was applied to produce drops of predetermined size and velocity in order to have well-defined conditions at the collision point.
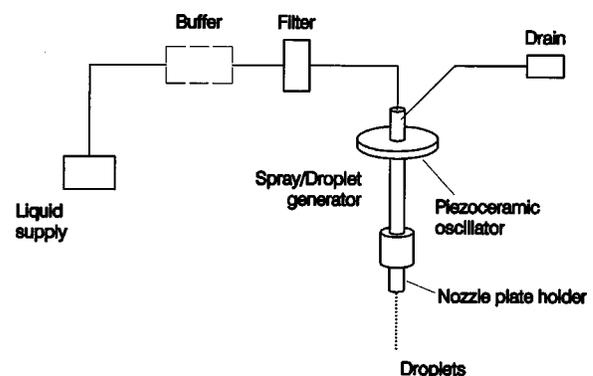

FIG. 2. Drop generator used for the production of monodisperse streams of drops. Two such devices were used for the experiments.
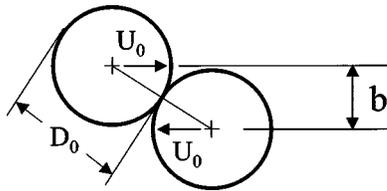
FIG. 3. The kinetic and geometric parameters of the collision.

The two drop generators providing the two streams of drops were fixed on a four-axis traverse. This traverse enabled an accurate 3D positioning of the two drop generators relative to the measuring control volume of the phase-Doppler anemometer. The fourth axis enabled the relative positioning of the two drop generators in the direction vertical to the plane of Fig. 1. This traverse enables the two drop streams to be placed at a well-defined distance of closest approach of the drop centers (for controlling the impact parameter), and to traverse the whole arrangement relative to the PDA probe volume for measuring at arbitrary locations in the flow field between the interacting drop streams. Furthermore, it was possible to change the intersection angle β between the two streams. All collisional interactions between the drops were produced symmetrical to the plane of Fig. 1. To achieve this, it was necessary to make sure that the two liquid jets emerged from the nozzles in directions normal to the nozzle plates. This was ensured by filtering the liquid in order to remove particulate impurities. In the present experiments it was possible to maintain stable liquid flow conditions through the drop generators for many hours.

The kinetic and geometric parameters determining the binary drop collision are shown in Fig. 3. The physical parameters of the liquid are the density ρ, the dynamic viscosity μ, and the surface tension σ. The size of the colliding drops is D_0, the relative velocity $2U_0$, and the impact parameter b. Using these parameters, the Weber number

$$\text{We} = \frac{\rho D_0 4 U_0^2}{\sigma},$$ (5)

the Ohnesorge number

$$Z = \frac{\mu}{\sqrt{\sigma D_0 \rho}},$$ (6)

and the nondimensional impact parameter

$$X = \frac{b}{D_0}$$ (7)

are defined. The influence of the Ohnesorge number is not considered in the present article, since only one test fluid was investigated.

B. The phase-Doppler anemometer

The measuring system used for the experiments was a one-component phase-Doppler anemometer (PDA). The system is sketched in Fig. 1 as a part of the whole test rig. The PDA was run with a HeNe laser. Important data of the PDA are the off-axis angle of 60°, the transmitting lens focal

length of 80 mm, the beam distance of 5.04 mm, and the Avalanche photodiode (APD) elevation angles of ±3.69°. Since all collisional interactions were produced symmetrical to the plane of the drop streams and the velocity direction in the drop streams was known beforehand, it sufficed to measure only one velocity component of the drops. Velocities normal to the plane due to angular momentum are very small and may be disregarded in the present investigations.

The Doppler signals were processed using a cross-spectral density routine on a personal computer, as presented by Domnick et al.[15] The output data were phase shifts and Doppler frequencies for each sample drop, and mean burst rates for groups of 100 samples. From these data, drop size and velocity were determined, and the burst rate was used to check the frequency of drop formation which was expected to equal the vibration frequency of the piezoceramic oscillators of the drop generators.

C. The visualization system

The plane of the interacting drop streams (which, strictly speaking, do not lie in one plane for impact parameters $b \neq 0$) was visualized by backlighting with a high-intensity LED and a CCD video camera. The electrical signal for driving the LED was synchronized with the signal that excited the drop generators. As a result, standing pictures of the drop streams were obtained. The observed processes were recorded on video tape, and photographs were taken from selected frames. The visualization system was used for surveying the whole variety of drop collision phenomena, for counting numbers of satellite droplets formed after stretching separation and disintegration of filaments, for determining the distance from the impact point where drop oscillations had died out and the drops had returned to their spherical shape, and for measuring lengths of filaments and time scales for filament pinch-off and satellite droplet formation. The latter feature was achieved by mutually phase shifting the signal for the drop formation and the control signal for the LED. This phase shift was measured as a time delay between the two signals on a digital storage oscilloscope. The delay was adjusted such that the video system showed just the start and the end of a certain process in question, and the time difference was determined.

D. The measurements

The measurements aimed at clarifying the influence of deterministic collisions between drops of two monodisperse streams on velocity and size of the drops downstream from the point of impact. The PDA measurements in the angular space between the two drop streams downstream from the point of intersection of the drop trajectories gave insight into the formation and breakup processes of drops after the collisions.

Propanol-2 was chosen as the test liquid for the experiments, because there are experimental reference data on the collisional behavior of propanol-2 drops available in the literature (Refs. 16 and 17), and the liquid is relevant for combustion research. The physical parameters of propanol-2 at 20 °C are given in Table I. Measurements were performed at

TABLE I. Properties of propanol-2 at a temperature of 20 °C. The refractive index is needed as an input parameter for the PDA measurements.

Dynamic viscosity μ (10^{-3} Pa·s)	Density ρ (kg/m^3)	Surface tension σ (10^{-3} N/m)	Refractive index m (−)
2.427	785.4	21.4	1.378

different flow rates determined by the driving pressure in the liquid reservoir and the orifice diameter, and different excitation frequencies applied to the drop generators. These variations resulted in different drop sizes and velocities at the point of impact.

Measurements with the PDA system were carried out at the intersection point in the undisturbed drop streams in order to determine the size and velocity of the colliding drops. Further measurement data were taken at appropriate positions downstream from the point of impact in order to quantify velocity and size of the new formed drops. According to their type, the collisions lead to permanent coalescence or to the formation of a complex drop with subsequent breakup. At each measuring point, 1000 samples were recorded in order to have statistically reliable results. This relatively small number of samples proved to be sufficient since the collisions took place between controlled droplets under controlled conditions, so that all droplets passing the probe volume at a given location in the flow field exhibited the same sizes and velocities with very small fluctuations.

The drop sizes investigated were varied between 68 and 123 μm by varying the excitation frequency and using orifices with the two different hole sizes mentioned earlier. Drop velocities in the direction of the drop streams ranged between 6.3 and 12.6 m/s. Due to the relative inclination β of the drop streams against each other between 26° and 44°, Weber numbers as defined in Eq. (5) in the range between 47 and 350 were achieved, which is relevant for many practical applications. Collisional interactions leading to shattering of the drops due to very high impact Weber numbers were not considered in the present work.

Before starting the PDA measurements, a series of visualization experiments was carried out. The results of these experiments are discussed in the following section.

III. RESULTS OF THE VISUALIZATION EXPERIMENTS

The visualization of the collisional interactions of the two monodisperse drop streams yielded information about the processes occurring after the collisions. All collisions, regardless of whether they are followed by permanent coalescence or by break-up, lead to deformations of the drops. The deformed drop shapes are unstable and converge to the spherical state by dampened oscillations of the drops. Locations in the flow field appropriate for PDA measurements were chosen such that these oscillations had died out and the drops were all spherical. The search for the right region for the PDA measurements in the light of this requirement was one important task for the visualization experiments, further to the phenomenological survey of the collision processes discussed subsequently.
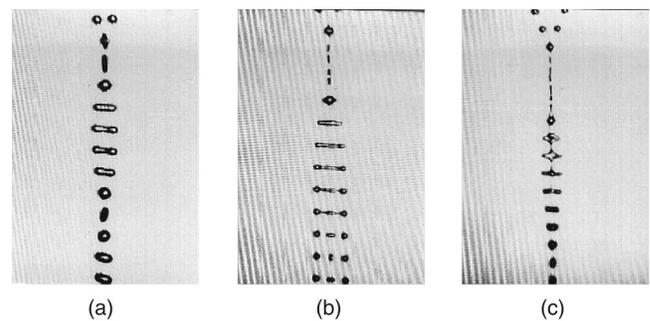

(a)   (b)   (c)

FIG. 4. Photographs of head-on collisions ($X=0$) of drops of equal size leading to a single new drop in (a) and (c), and to the formation of a big satellite droplet and two boundary drops in (b). (a) $D_0=105$ μm, We=49; (b) $D_0=121$ μm, We=132; (c) $D_0=114$ μm, We=177.

Figures 4(a)–4(c) show three examples of processes observed after head-on collisions ($X=0$) of drops with equal diameters. The main direction of motion of the drops on the photographs is downward. The collisions took place at the three different Weber numbers 49, 132, and 177. The drop diameters were 105, 121, and 114 μm. In Fig. 4(a) it is seen that, after the impact, the two drops merge and form one stable new drop. This is a case of permanent coalescence (We=49). With increasing impact Weber number, the surface energy of the complex drop does not suffice any more to keep the system stable. Therefore, after the formation of the complex drop, the new drop is first deformed to a flat disk and thereafter assumes the shape of a filament (We=132). This filament is unstable and breaks up to form one satellite droplet and two boundary drops, as seen in Fig. 4(b). A further increase of the impact Weber number to the value of 177 leads to a very large deformation of the complex drop right after the impact, as seen in Fig. 4(c). The deformation is of the order of the half distance between the drops in the interacting streams, so that, after the impact, neighboring drops come into contact with each other, merge, and form a structure like a liquid jet downstream from the point of impact. This jet again breaks up into droplets. The photograph shows no satellite production from the jet breakup, which may be caused by the fact that the jet is subject to forced periodic disturbances by the impacting drops, characterized by a wave number and disturbance amplitude where satellites do not occur. This process must be considered as an artifact and
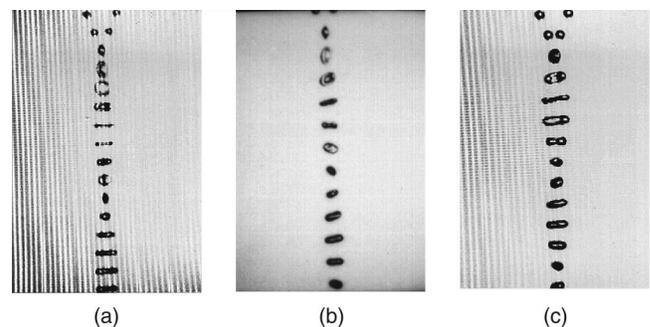

(a)   (b)   (c)

FIG. 5. Photographs of near-head-on collisions leading to stable coalescence of the drops: (a) $D_0=114$ μm, We=177, $X=0.175$; (b) $D_0=121$ μm, We=132, $X=0.165$; (c) $D_0=105$ μm, We=49, $X=0.357$.
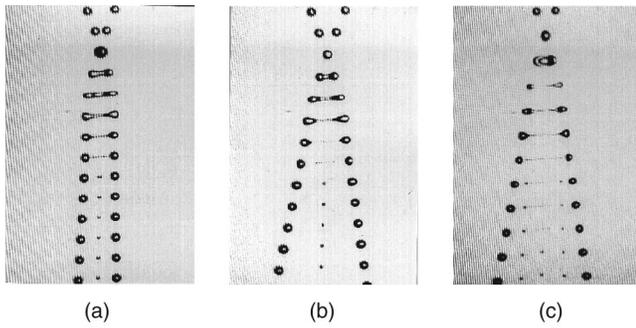
FIG. 6. Photographs of off-center collisions between pairs of drops with equal size of $D_0 = 105$ μm, We=49, and (a) X=0.53, (b) X=0.57, both leading to the formation of one satellite droplet; (c) drop size $D_0 = 121$ μm, We=132, X=0.44, leading to the formation of three satellite droplets.
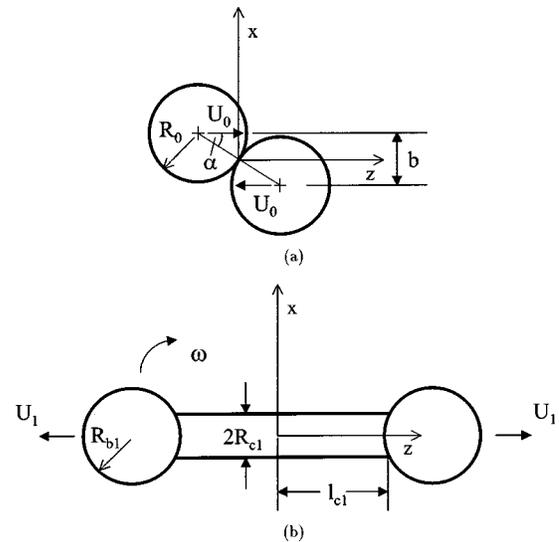

FIG. 7. Geometrical and dynamic properties of the drops (a) at the first instant of impact and (b) during the stretching process after an off-center collision.

limitation to the present experimental technique, caused by the periodical arrival of drops at the point of impact at a limited (and well defined) interdrop distance. Therefore we do not investigate this phenomenon.

Figures 5(a)–5(c) show three different cases of near-head-on collisions which lead to drop coalescence. The colliding drops exhibit small impact parameters, which are characterized by the nondimensional values of 0.175, 0.165, and 0.357 in Figs. 5(a), 5(b), and 5(c), respectively. The Weber numbers and the drop diameters were the same as in Fig. 4. The drops exhibit an angular momentum before the collision, which leads to a rotation of the coalesced drops after the collision. At the same time, the new formed drops exhibit shape oscillations, so that the combined motion of these drops is a superposition of these two interacting contributions.

In Figs. 6(a)–6(c) we present photographs of stretching separation. Figures 6(a) and 6(b) show collisions which lead to the formation of one satellite droplet at the impact Weber number of 49 and the different nondimensional impact parameters X=0.53 and 0.57. After the collision, a filament connecting the two boundary drops is formed. After five periods of the signal applied to produce the colliding drops, this filament separates from the bulbous ends (which consist of the remainders of the colliding drops), and contracts into a small satellite droplet in the center of the drop arrangement. In Fig. 6(c) the case of a collision leading to three satellite droplets is shown. This case is characterized by the larger impact Weber number We=132 and the intermediate impact parameter X=0.44. The higher kinetic energy of the drops allows for the formation of a longer filament in this case, and hence more than one satellite is formed. The odd number of satellites is characteristic for the formation process called "end pinching," which is visible in Fig. 6(c).

IV. MODEL FOR FILAMENT BREAKUP AFTER HEAD-ON AND OFF-CENTER COLLISIONS

The model presented in this section was developed in order to predict the number and size of satellite droplets formed by filament breakup after unstable head-on or off-center collisions. We consider a collision of two drops of equal size, looking at the more general off-center case. The results can then be specialized to describe the head-on case of vanishing impact parameter b.

The configurations of the drops at the first instant of the impact and in an intermediate state of deformation of the complex drop after the collision are sketched in Figs. 7(a) and 7(b). The state in Fig. 7(a) is denoted by subscript "0," the state in Fig. 7(b) by subscript "1." In order to describe the breakup processes, we will apply a linear stability analysis. For the basic state we choose the configuration in Fig. 7(b). For calculating the physical parameters characterizing this basic state, we look at the overall balances of mass, energy, and angular momentum.

The whole process is assumed to take place in the x,z plane of the Cartesian coordinate system $Oxyz$ in Fig. 7. The center of the system is fixed with the center of gravity of the two drops. Before the impact, the size of the colliding drops is $D_0 = 2R_0$, and their velocity relative to the coordinate system is U_0, which in our case is oriented along the z axis. At the instant after the collision depicted in Fig. 7(b), the complex drop consists of the masses of the two boundary drops with radius R_{b1}, and a cylinder with radius R_{c1} and length $2l_{c1}$. The fluid is considered as incompressible, and effects of evaporation or condensation are not taken into account. Therefore, the volumes before and after the collision are equal:

$$2 \cdot \tfrac{4}{3}\pi R_0^3 = \tfrac{2}{3}\pi (R_{b1} + \sqrt{R_{b1}^2 - R_{c1}^2})^2$$

$$\times (2R_{b1} - \sqrt{R_{b1}^2 - R_{c1}^2}) + 2\pi R_{c1}^2 l_{c1}. \tag{8}$$

This equation relates the geometrical parameters of the system before and at the intermediate instant after the collision.

In the state before the impact, the total energy E_0 of the drops, composed of kinetic and surface energies, is

Phys. Fluids, Vol. 13, No. 9, September 2001

Satellite droplets from drop collisions   2469

$$E_0 = 2 \cdot \left(\frac{1}{2} \rho \frac{4}{3} \pi R_0^3 U_0^2 + 4\pi R_0^2 \sigma \right)$$

$$= 4\pi R_0^2 \left(\rho \frac{R_0 U_0^2}{3} + 2\sigma \right). \tag{9}$$

This result is of course independent of the impact parameter.

At the instant of impact depicted in Fig. 7(a), the angular momentum of the two drops has only one nonvanishing Cartesian component—in the y direction of the coordinate system. This component of the vector reads

$$L_{0,y} = 2\rho U_0 \int_V x \, dV, \tag{10}$$

where V is the volume of the fluid and ρ is its density. In order to solve this integral, it is convenient to first translate the origin of the coordinate system into the center of one of the drops, e.g., of the left drop in Fig. 7(a), by the transformation $x_1 = x - R_0 \cos \alpha$, $y_1 = y$, $z_1 = z + R_0 \sin \alpha$ [where $\cos \alpha = b/(2R_0)$], and then to transform the Cartesian system into a spherical one. The final result reads

$$L_{0,y} = \tfrac{4}{3} \pi \rho U_0 R_0^3 b. \tag{11}$$

In Eq. (11), b denotes the dimensional impact parameter sketched in Fig. 7(a).

We must now formulate the total energy E_1 and the angular momentum $\vec{L}_1$ at the intermediate instant "1" after the impact sketched in Fig. 7(b). The kinetic and surface energies of the drop system at this instant are calculated by the equations

$$E_{\text{kin},1} = \frac{4}{3} \pi R_{b1}^3 \rho [U_1^2 + \omega^2 (l_{c1} + R_{b1})^2] + \frac{\rho}{2} \int_{V_c} u^2 \, dV \tag{12}$$

and

$$E_{s,1} = \sigma \cdot S = 4\pi \sigma R_{c1} l_{c1} + 4\pi \sigma R_{b1}(R_{b1} + \sqrt{R_{b1}^2 - R_{c1}^2}), \tag{13}$$

where U_1 is the translational velocity of the bulbous end drops, $\vec{u}$ is the velocity of the fluid in the cylindrical filament, and ω is the angular velocity. The fluid velocity $\vec{u}$ is a superposition of a translational and a rotational motion. The interfaces of the complex drop are fully mobile. Therefore it follows from the theorem of conservation of vorticity that the motion in the complex is free of vorticity. Then the z component of the translational velocity is represented as $u_{t,z} = U_1 z / l_{c1}$. Since the complex rotates around the y axis of the coordinate system, the components of the rotational velocity are $(u_{r,x}, u_{r,y}, u_{r,z}) = (-\omega z, 0, \omega x)$.

From the geometry of the system sketched in Fig. 7(b) it may be concluded that, for some calculations, it is convenient to use the cylindrical coordinate system $Or\vartheta z$. The center of this coordinate system coincides with the center of the Cartesian one, and r, ϑ, and z are the cylindrical coordinates. The transformation into the Cartesian frame reads

$$x = r \cos \vartheta, \quad y = r \sin \vartheta, \quad z = z. \tag{14}$$

Then, from the continuity equation $\nabla \cdot \vec{u} = 0$, the radial component of the translational velocity may be calculated as $u_{t,r} = -U_1 r/(2l_{c1})$. The components of the fluid velocity $\vec{u}$ in the cylindrical filament now read

$$(u_x, u_y, u_z) = \left(-\frac{U_1 x}{2l_{c1}} - \omega z, -\frac{U_1 y}{2l_{c1}}, \frac{U_1 z}{l_{c1}} + \omega x \right) \tag{15}$$

and

$$(u_r, u_\vartheta, u_z)$$
$$= \left(-\frac{U_1 r}{2l_{c1}} - \omega z \cos \vartheta, \omega z \sin \vartheta, \frac{U_1 z}{l_{c1}} + \omega z \cos \vartheta \right) \tag{16}$$

in the Cartesian and the cylindrical frames, respectively. Using this velocity distribution, the kinetic energy at instant "1" after the impact reads

$$E_{\text{kin},1} = \frac{4}{3} \pi R_{b1}^3 \rho [U_1^2 + \omega^2 (l_{c1} + R_{b1})^2]$$
$$+ \frac{\pi \rho U_1^2 R_{c1}^2}{l_{c1}} \left(\frac{R_{c1}^2}{8} + \frac{l_{c1}^2}{3} \right)$$
$$+ \pi \rho \omega^2 R_{c1}^2 l_{c1} \left(\frac{R_{c1}^2}{4} + \frac{l_{c1}^2}{3} \right). \tag{17}$$

From Eqs. (13) and (17) we obtain the total energy at instant "1":

$$E_1 = 4\pi \sigma R_{c1} l_{c1} + 4\pi \sigma R_{b1}(R_{b1} + \sqrt{R_{b1}^2 - R_{c1}^2})$$
$$+ \frac{4}{3} \pi R_{b1}^3 \rho [U_1^2 + \omega^2 (l_{c1} + R_{b1})^2]$$
$$+ \frac{\pi \rho U_1^2 R_{c1}^2}{l_{c1}} \left(\frac{R_{c1}^2}{8} + \frac{l_{c1}^2}{3} \right)$$
$$+ \pi \rho \omega^2 R_{c1}^2 l_{c1} \left(\frac{R_{c1}^2}{4} + \frac{l_{c1}^2}{3} \right). \tag{18}$$

The angular momentum of the liquid system at instant "1" in Fig. 7(b) can be represented as the sum of the contributions $L_{c1,y}$ from the cylindrical filament and $L_{b1,y}$ from the bulbous ends of the system, which read

$$L_{c1,y} = \rho \int_\vartheta \int_z \int_r \left(\frac{U_1 z r}{2l_{c1}} \cos \vartheta + \omega r^2 \cos^2 \vartheta + \omega z^2 \right) r \, dr \, dz \, d\vartheta$$
$$= 2\pi \rho \omega l_{c1} R_{c1}^2 \left(\frac{R_{c1}^2}{4} + \frac{l_{c1}^2}{3} \right) \tag{19}$$

and

$$L_{b1,y} = 2\rho \int_V (\vec{u} \times \vec{r})_y \, dV$$
$$= 2\rho \int_V (u_z x - u_x z) \, dV$$
$$= \frac{8}{3} \pi \rho \omega R_{b1}^3 \left[(l_{c1} + R_{b1})^2 + \frac{2}{5} R_{b1}^2 \right], \tag{20}$$

respectively. The total angular momentum after the collision is therefore

$$L_{1,y} = 2\pi\rho\omega l_{c1}R_{c1}^2\left(\frac{R_{c1}^2}{4} + \frac{l_{c1}^2}{3}\right)$$

$$+ \frac{8}{3}\pi\rho\omega R_{b1}^3\left[(l_{c1}+R_{b1})^2 + \frac{2}{5}R_{b1}^2\right]. \quad (21)$$

For further calculations, these equations are nondimensionalized by dividing lengths by the initial drop radius R_0, except the impact parameter b, which is rendered nondimensional by $D_0 = 2R_0$. The velocities are nondimensionalized by U_0, the angular velocity by U_0/R_0. The Weber number and the nondimensional parameters are defined as follows:

$$\text{We} \equiv \frac{\rho D_0 4 U_0^2}{\sigma}, \quad \tilde{l}_c \equiv \frac{l_{c1}}{R_0}, \quad \tilde{R}_b \equiv \frac{R_{b1}}{R_0}, \quad \tilde{R}_c \equiv \frac{R_{c1}}{R_0},$$

$$\tilde{U} \equiv \frac{U_1}{U_0}, \quad \tilde{\omega} \equiv \frac{\omega R_0}{U_0}. \quad (22)$$

This leads to the following nondimensional form of the mass, angular momentum, and energy balances:

$$\frac{1}{3}(\tilde{R}_b + \sqrt{\tilde{R}_b^2 - \tilde{R}_c^2})^2(2\tilde{R}_b - \sqrt{\tilde{R}_b^2 - \tilde{R}_c^2}) + \tilde{R}_c^2\tilde{l}_c = \frac{4}{3}, \quad (23)$$

$$\tilde{\omega}\left\{2\tilde{R}_c^2\tilde{l}_c\left(\frac{\tilde{R}_c^2}{4} + \frac{\tilde{l}_c^2}{3}\right) + \frac{8}{3}\tilde{R}_b^5\left[\left(\frac{\tilde{l}_c}{\tilde{R}_b} + 1\right)^2 + \frac{2}{5}\right]\right\} = \frac{8}{3}X, \quad (24)$$

$$\frac{\text{We}}{48}\tilde{U}^2\tilde{R}_b^3\left[1 + \frac{\tilde{\omega}^2}{\tilde{U}^2}(\tilde{l}_c + \tilde{R}_b)^2 + \frac{\tilde{\omega}^2}{\tilde{U}^2}\frac{3\tilde{R}_c^2\tilde{l}_c^3}{4\tilde{R}_b^3}\left(\frac{1}{3} + \frac{\tilde{R}_c^2}{4\tilde{l}_c^2}\right)\right.$$

$$\left. + \frac{3\tilde{R}_c^2}{4\tilde{R}_b^3\tilde{l}_c}\left(\frac{\tilde{R}_c^2}{8} + \frac{\tilde{l}_c^2}{3}\right)\right]$$

$$+ \frac{\tilde{R}_c\tilde{l}_c}{2} + \frac{\tilde{R}_b^2}{2}\left(1 + \frac{\sqrt{\tilde{R}_b^2 - \tilde{R}_c^2}}{\tilde{R}_b}\right) = \frac{\text{We}}{48} + 1. \quad (25)$$

If the Weber number and two of the three geometrical parameters $\tilde{R}_b$, $\tilde{R}_c$, and $\tilde{l}_c$ are known, the third geometrical parameter, the nondimensional velocity $\tilde{U}$, and the nondimensional angular velocity $\tilde{\omega}$ can be calculated. Numerical calculations show that the ratio of the nondimensional angular and translational velocities $(\tilde{\omega}/\tilde{U}) \ll 1$, so that all terms proportional to the square of this ratio can be neglected. This means that, from the dynamic point of view, the process of liquid filament disintegration after off-center drop collisions can be treated as with head-on collisions, provided that the filament volume is represented correctly. This result is in agreement with the findings of Ashgriz and Poo[1] who reported physical evidence for the fact that a rotational motion cannot play a significant role in the dynamics of stretching separation after unstable binary drop collisions.

In order to investigate the stability of the complex drop after the collision sketched in Fig. 7(b), we now apply a linear stability analysis. For performing this analysis of the system, we introduce small perturbations of the basic state—for the shape $h(z,t)$, and for the velocity $u^1(r,z,t)$. In Fig. 8 the shape perturbations on the complex are
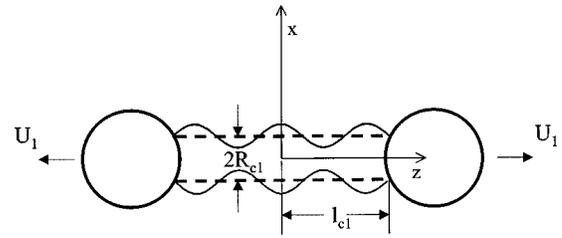

FIG. 8. Geometrical disturbances on the filament between the boundary drops as described in the present model.

sketched. We assume that the physically possible shapes are wave-like, with a half-wave ending at the ends of the cylinder. Therefore, the perturbations affect only the liquid velocity and the radius of the filament. The perturbations in the shape and velocity are superimposed to the basic state to yield

$$u \to u + u^1, \quad R_c \to R_c + h(z,t). \quad (26)$$

Since the motion of the fluid is irrotational, the velocity field in the basic state is potential $(u_r = -U_1 r/2l_c, u_z = U_1 z/l_c)$, and it can be described as the gradient $\nabla\varphi$ of a potential function φ which satisfies the Laplace equation. The fluctuation of the potential function caused by the perturbations is denoted as φ^1. It is a solution of the first integral of the equation of motion:

$$\frac{\partial\varphi^1}{\partial t} + u \cdot u^1 + \frac{p^1}{\rho} = 0, \quad (27)$$

where p^1 is the pressure disturbance arising from the geometrical deformation of the filament. In a cylindrical frame with axisymmetry around the z axis, the Laplace equation has the general solution

$$\varphi^1 = C(t) \cdot I_0\left(k\frac{r}{l_c}\right) \cdot \cos\left(k\frac{z}{l_c}\right), \quad (28)$$

where $C(t)$ is the time-dependent amplitude of the potential, I_0 is the zeroth-order modified Bessel function of the first kind, and $k = 2\pi l_c/\lambda$ is the nondimensional wave number. We assume that, at the ends $z = \pm l_c$ of the cylinder, the wave is continuous, as sketched in Fig. 8. In order to specify the above solution for the velocity potential for the present problem, the amplitude function $C(t)$ must be determined. The solution of our problem is subject to dynamic and kinematic boundary conditions, which read in linear form

$$p^1 + \sigma\left(\frac{\partial^2 h}{\partial z^2} + \frac{h}{R_c^2}\right) = 0 \quad \text{and} \quad \frac{\partial h}{\partial t} + u_z\frac{\partial h}{\partial z} = u_r^1$$

$$\text{at} \quad r = R_c. \quad (29)$$

The convective term in the kinematic boundary condition depends on the z coordinate. In order to avoid this difficulty, we make the following transformation of variables:

$$\tau = t, \quad \zeta = f(t) \cdot z, \quad (30)$$

where $f(t)$ is a function depending only on t, which we choose as a solution of the ordinary differential equation $d\ln f/dt = -U_1/l_c$. This transformation reduces the problem to

Phys. Fluids, Vol. 13, No. 9, September 2001

Satellite droplets from drop collisions   2471

$$\frac{\partial \varphi^1}{\partial \tau} - \frac{U_1 r}{2l_c} \frac{\partial \varphi^1}{\partial r} + \frac{p^1}{\rho} = 0, \tag{31}$$

$$\frac{\partial h}{\partial \tau} = u_r^1. \tag{32}$$

Using Eq. (29), the pressure disturbance p^1 is eliminated from Eq. (31). The equation obtained from this elimination is then differentiated with respect to τ, and with the use of Eq. (32) we obtain the following Eulerian ordinary differential equation (ODE) of second order in the amplitude function $C(\tau)$:

$$\frac{d^2 C}{d\tau^2} - \frac{k\tilde{U}\tilde{R}_c^2}{2\tilde{l}_c} \frac{I_{1,c}}{I_{0,c}} \frac{dC}{d\tau} + \frac{8}{\text{We}\tilde{R}_c^2 \tilde{l}_c} \left(k^3 \frac{\tilde{R}_c^2}{\tilde{l}_c^2} - k \right) \frac{I_{1,c}}{I_{0,c}} C(\tau) = 0, \tag{33}$$

where $I_{0,c} = I_0(k\tilde{R}_c/\tilde{l}_c)$ and $I_{1,c} = I_1(k\tilde{R}_c/\tilde{l}_c)$. This equation has solutions of the form

$$C(\tau) = A \cdot \exp(\lambda \tau) \tag{34}$$

with the constant A, which are substituted into the ODE (33) to yield the characteristic equation of the ODE. This equation has the two solutions

$$\lambda_{1,2} = (k\tilde{U}\tilde{R}_c^2/4\tilde{l}_c)(I_{1,c}/I_{0,c}) \pm \tfrac{1}{2}\sqrt{B}, \tag{35}$$

where B represents the expression

$$B = \frac{k^2 \tilde{U}^2 \tilde{R}_c^4}{4\tilde{l}_c^2} \left(\frac{I_{1,c}}{I_{0,c}} \right)^2 - \frac{32}{\text{We}\tilde{R}_c^2 \tilde{l}_c} \left(k^3 \frac{\tilde{R}_c^2}{\tilde{l}_c^2} - k \right) \frac{I_{1,c}}{I_{0,c}}. \tag{36}$$

The perturbations on the filament are periodic in time when B is negative, and they grow exponentially when B is positive. We therefore seek for solutions of our equations where B just changes its sign, i.e., $B = 0$. At this state we calculate the (critical) nondimensional filament radius $\tilde{R}_{c,cr}$ as a function of the wave number k. The wave number has a discrete spectrum and can assume only values $k = n\pi/2$ with $n = 1, 2, \ldots$. The different values of k correspond to different numbers of satellite droplets formed after the collision. The number of satellite droplets depends very strongly on the type of collision (head-on or off-center), and on the Weber number. The results for $\tilde{R}_{c,cr}$ as a function of the Weber number in the case of a head-on collision are plotted in Fig. 9 for five different values of the wave number k. The curves divide the graph into zones of stable and unstable filament behavior. In the zones above the curves (i.e., for filaments thicker than given by the curves), the filament is stable against the disturbances. Thinner filaments are unstable. This graph is an important basis for the prediction of the number of satellite droplets formed by the filament breakup.

For the instability of the filament, not all wave numbers are equally important. The disturbances with different wave numbers represent different disturbance energies. It is our next aim to calculate the energy of the disturbances. The wave number of the disturbance with the largest energy will be made responsible for the satellite formation by filament breakup.
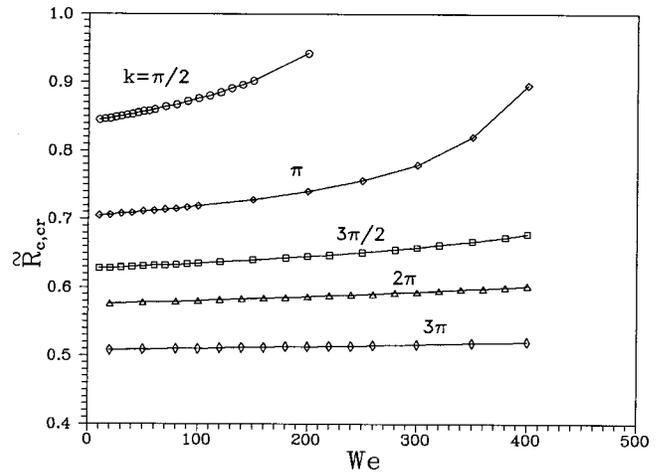

FIG. 9. The stability behavior of filaments against disturbances with the wave number k. The filaments are characterized by the nondimensional critical radius $\tilde{R}_{c,cr}$, where instability sets in. They are produced by binary collisions of drops with the impact Weber number We. States below the curves are unstable.

The energy of the disturbances is the difference between the total energies of the disturbed system and the unperturbed state. This energy is composed of contributions of surface and kinetic energies. The variation of the surface energy is proportional to the square of the disturbance amplitude, so that the contribution of the surface energy to the total disturbance energy is zero. The energy of the disturbances is therefore represented by the kinetic contribution only, which is calculated in approximation to first order by the equation

$$E_d = \Delta E_{\text{kin}} = \int_0^{R_{c1}} \int_{-l_{c1}}^{l_{c1}} \rho u u^1 r \, dr \, dz$$

$$= \frac{\rho U_1 R_{c1}}{k} (2l_{c1} I_{1,c} \cos k - R_{b1} I_{0,c} \sin k) \cdot C(t). \tag{37}$$

For numerical calculations it is convenient to normalize E_d with the total energy E_0 of the unperturbed state, which results in

$$\tilde{E}_d = \frac{E_d}{E_0} = \frac{3\text{We}\tilde{U}\tilde{R}_c \tilde{l}_c}{4\pi k(\text{We}+48)}$$

$$\times \left(2I_{1,c} \cos k - \frac{\tilde{R}_c}{\tilde{l}_c} I_{0,c} \sin k \right) \cdot \tilde{C}, \tag{38}$$

where $\tilde{C} = C/(U_0 R_0)$.

In general the processes of filament stretching and break-up are complicated, and the assumption that disturbances do not affect the bulbous ends of the complex drop does not always hold. Therefore, in the following sections we consider only two particular cases: head-on collisions and unstable off-center collisions with large enough impact parameter. For intermediate values of the impact parameter, the present model cannot give correct predictions.
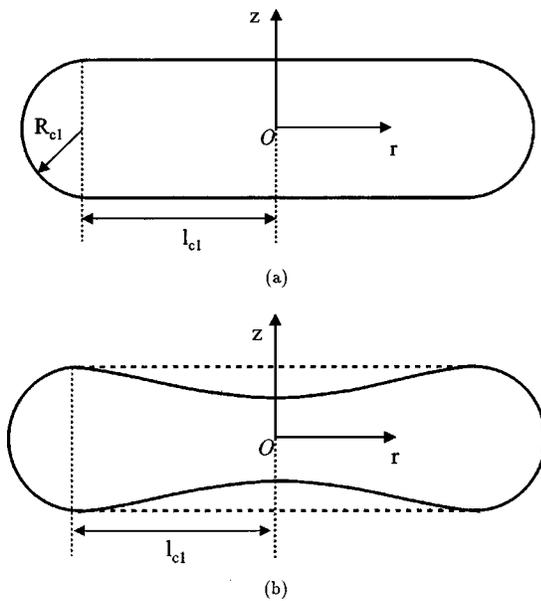
FIG. 10. Geometrical configurations of the complex drop after (a) head-on and (b) off-center collisions.

A. Head-on collisions

After a head-on collision ($X=0$), the radius of the ends of the complex drop may be assumed to equal the radius of the cylinder, i.e., $R_{b1}=R_{c1}=R_1$. The configuration of the complex drop at instant "1" after the head-on collision is sketched in Fig. 10(a). Then Eqs. (23)—(25), which determine the basic state of the system, reduce to

$$\tfrac{2}{3}\widetilde{R}_1^3 + \widetilde{R}_1^2\widetilde{l}_c = \tfrac{4}{3}, \tag{39}$$

$$\frac{\text{We}}{48}\widetilde{U}^2\widetilde{R}_c^2\widetilde{l}_c\left(\frac{1}{4}+\frac{\widetilde{R}_c}{2\widetilde{l}_c}+\frac{3\widetilde{R}_c^2}{32\widetilde{l}_c^2}\right)+\frac{\widetilde{R}_c\widetilde{l}_c}{2}+\frac{\widetilde{R}_c^2}{2}=\frac{\text{We}}{48}+1. \tag{40}$$

With the help of these equations, the critical radius of the cylinder can be determined from Eq. (36) for $B=0$ and for a given wave number k.

According to the work of Ashgriz and Poo,[1] the first unstable configuration with the formation of two drops after the collision, as seen in Fig. 3 of their paper, corresponds to $k=\pi/2$. The disturbance waves are fixed at the ends of the cylindrical part, and the first mode looks as sketched in Fig. 10(b). Also, $k=\pi$ corresponds to the formation of three drops, and so on. In order to determine which wave number is responsible for the breakup of the filament, the energy of the perturbations is calculated from Eq. (38).

B. Off-center collisions

From our experimental results, which will be presented in the next section, it is seen that, in the case of off-center collisions, the following assumptions for the instant of maximum possible deformation of the complex drop (just before break-up) can be made:

(i)   the radius of the cylinder is much smaller than the radius of the bulbous ends ($\widetilde{R}_c/\widetilde{R}_b \ll 1$), and

(ii)   the length of the filament is much larger than the radius of the bulbous ends, which is expressed mathematically by $(\widetilde{l}_c/\widetilde{R}_b+1)^2 \gg \tfrac{2}{5}$.

Under these conditions, Eqs. (23)–(25) reduce to

$$\tfrac{4}{3}\widetilde{R}_b^3 + \widetilde{R}_b^2\widetilde{l}_c = \tfrac{4}{3}, \tag{41}$$

$$\frac{\text{We}}{64}\widetilde{U}^2\left(\frac{4}{3}\widetilde{R}_b^3+\frac{\widetilde{R}_c\widetilde{l}_c}{3}\right)+\frac{\widetilde{R}_c\widetilde{l}_c}{2}+\widetilde{R}_b^2=\frac{\text{We}}{48}+1. \tag{42}$$

In the case of off-center collisions, the perturbation waves on the cylindrical filament are also fixed to the ends of the filament. The filament ends, which are attached to the boundary drops, are always unstable regions, because the bulbous end drops have higher inertia and, due to a necking process, the filament tends to detach from these bulbs. Therefore, the first unstable case, where $k=\pi/2$, here corresponds to the formation of one satellite droplet and the two boundary drops after the collision. Equally, $k=3\pi/2$ corresponds to the formation of two satellites, i.e., of overall four drops, $k=5\pi/2$ forms three satellites, and so on. It is important to note that the interpretation of the wave number and the overall number of drops produced after the collision is different for the cases of head-on and off-center collisions. Again, in order to confirm which value of k is responsible for the break-up, we calculate the energy of the fluctuations.

In the following section we will test the results from the present model against experimental data.

V. EXPERIMENTAL AND COMPUTATIONAL RESULTS

A. Experimental observations on binary drop collisions

In our experiments, the collisional interaction of pairs of propanol-2 drops from two monodisperse streams was studied. The experimental results of binary collisions between droplets with equal size D_0 are plotted in Figs. 11 and 12. In Fig. 11 the data for drops produced with 30 μm orifices are
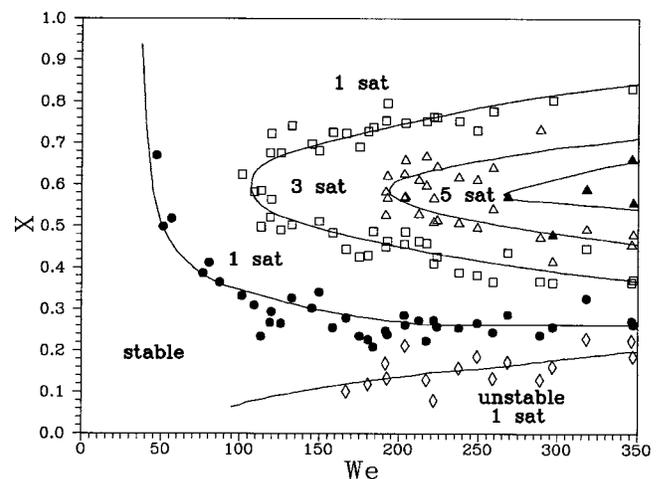

FIG. 11. Stability nomogram. Experimental data for the collision of drops with equal sizes produced by 30 μm orifices. The regimes of separation after unstable head-on or near-head-on collisions, permanent coalescence, and formation of one, three, five, and seven satellite droplets are shown. The regimes of a constant number of satellite droplets are clearly separated.
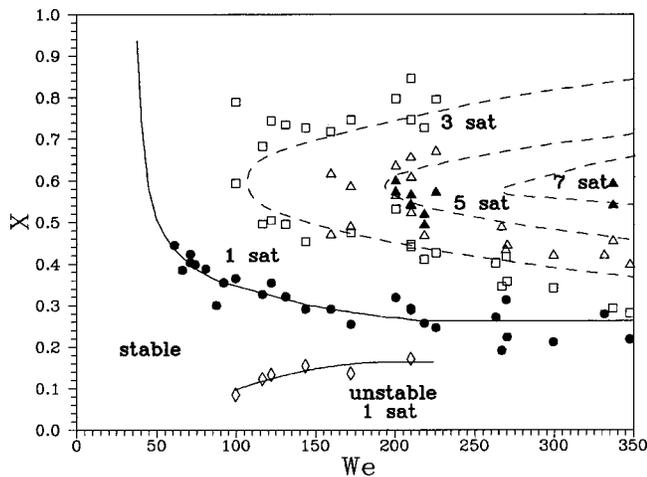
FIG. 12. Stability nomogram. Experimental data for the collision of drops with equal sizes produced by 50 μm orifices. The regimes of separation after unstable head-on or near-head-on collisions, permanent coalescence, and formation of one, three, five, and seven satellite droplets are shown. The stability limit against stretching separation and the dashed boundaries of regimes were determined with the data of Fig. 11.

presented, and in Fig. 12 those for 50 μm orifices. These nomograms exhibit for the first time the shapes of zones with constant numbers of satellite droplets produced after stretching separation. For both cases the Weber numbers ranged between 50 and 350, and nondimensional impact parameters X between 0 and 1 were realized. The diameters of the droplets varied between 68 and 107 μm for the 30 μm orifices, and between 103 and 123 μm for the 50 μm orifices. The Weber number was calculated according to Eq. (5). The curves marked with filled circles show the stability limit, which is the boundary between zones of coalescence and the unstable regime of stretching separation with formation of a single satellite droplet, as shown in the photographs in Figs. 5–6(b). Below this line (i.e., for smaller impact parameter) two different regimes are found. One of them is the permanent coalescence regime, illustrated by the collision in Fig. 4(a). In this regime, the two colliding drops merge to form a larger one. According to the correlation by Jiang *et al.*,[6] the second regime, where reflexive separation occurs and collisions are therefore unstable, appears at a Weber number We_c of about 40.3 for propanol-2. This value was deduced from the data in Fig. 10 of Jiang *et al.* Our observation of this phenomenon in a range of Weber numbers greater than 150 for the drops from the 30 μm orifices, and greater than 100 for the 50 μm orifices, and for low nondimensional impact parameters X from 0 to 0.2 (below the open diamonds), is in agreement with Jiang *et al.*'s results. This case of reflexive separation after unstable head-on and near-head-on collisions is shown in Fig. 4(b). The reflexive separation produces two boundary droplets and a big satellite between them. Head-on and near-head-on collisions usually lead to strong deformations of the droplets, which become stronger with increasing impact Weber number. The deformations may become so strong that, in the present experiments, the drops come into contact with each other after the collision and form a coherent structure. Figure 4(c) shows such a case. This is an artifact caused by the experimental technique, which would in

reality occur only in sprays with extremely high spatial drop concentration. This artifact puts limits to the range of Weber numbers we can investigate in our experiments.

In Fig. 11, the line marking the stability limit against stretching separation and the lines separating the regimes of formation of different numbers of satellite droplets were determined according to the data in Fig. 11 and then drawn in Fig. 12 also, together with the experimental data for collisions of drops from the 50 μm orifices. This allows for a comparison of the regimes for the different colliding drop sizes. We see that the stability limits against stretching separation coincide in both nomograms. We see no influence of the absolute drop size on this part of the experimental results. For impact parameters above the stability limit, different types of stretching separation were observed, which lead to the formation of various numbers of satellite droplets by filament breakup. The actual number of satellite droplets produced depends on the Weber number and the impact parameter. For We between 0 and 100, only one small satellite droplet is produced [see Figs. 6(a) and 6(b)]. It is seen that in this region the nondimensional impact parameter, at which the onset of formation of a single satellite droplet by stretching separation is observed, decreases with increasing Weber number. For Weber numbers $We > 200$ the nondimensional impact parameter marking the stability limit against stretching separation remains approximately constant. When a threshold value of We of about 100 is exceeded, the formation of three satellite droplets after the collision starts [see Fig. 6(c)]—provided that the impact parameter is sufficiently large. The open squares mark the boundary between the regions with formation of one and three satellite droplets after stretching separation. A further increase of the impact parameter may lead to the formation of five satellite droplets, if the impact Weber number is high enough. For the 30 μm orifices, this regime starts at the Weber number of around 180, while it begins at a Weber number around 150 for the 50 μm orifice. The open upward pointing triangles mark the boundary between the zones with three and five satellite droplets. A further increase of the impact parameter above values of about 0.7 at We$\approx$240 again leads to the formation of three and, for even larger impact parameters, to a single satellite droplet. Larger impact Weber numbers above 260 with impact parameters $X\approx0.6$ lead to the formation of seven satellites. This regime is depicted in Figs. 11 and 12 by the filled triangles. All regimes are clearly separated in both nomograms. For the 50 μm orifices the regimes are slightly shifted towards smaller Weber numbers, as can be seen by comparing the locations of the symbols for the experimental results and the dashed lines in Fig. 12. The regimes are narrower in the case of the larger colliding drops, since the onset Weber numbers for the formation of a given number of satellite droplets are smaller than with smaller drops, shifting the regimes to the left in the nomogram.

Above the stability limit against stretching separation, the complex drop formed by the collision elongates due to inertia and forms a thin filament between the two large drop portions (boundary drops) at its ends. The filament finally pinches off the boundary drops and breaks up, producing one, three, or more satellite droplets, depending on the We-
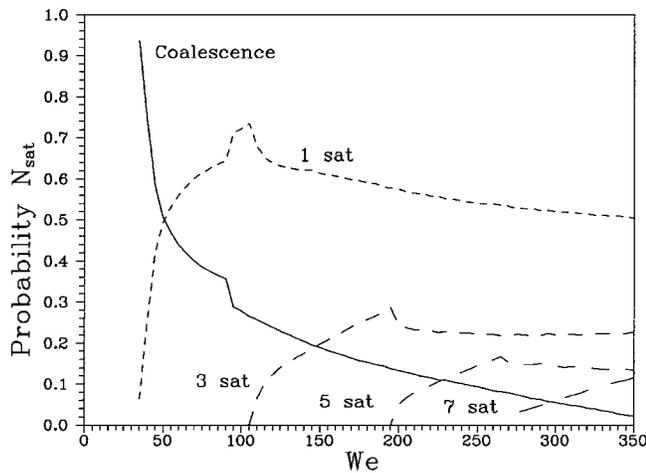
FIG. 13. The probability of formation of a given number of satellite droplets by unstable binary drop collisions as a function of the impact Weber number. The data were determined from Fig. 11.
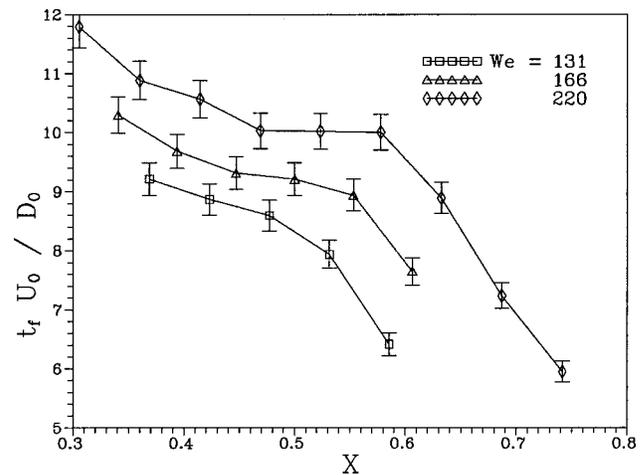

FIG. 14. The nondimensional time to filament pinch-off from the boundary drops as a function of the nondimensional impact parameter for different Weber numbers (error 3%).

ber number and the impact parameter, as quantified in Figs. 11 and 12. The probability of the formation of a given number of satellite droplets may be quantified on the basis of the above stability nomograms under the assumption that all impact parameters are equally probable. This has been done for the data in Fig. 11, and the results are shown in Fig. 13. The onset Weber numbers for the formation of the various numbers of satellites are clearly seen. The data show that the formation of just one single satellite droplet is most probable for the whole range of Weber numbers investigated. This is the motivation for looking more closely at the details of this process in the following section.

B. The process of stretching separation

In order to quantify the process of satellite droplet formation by filament disintegration after stretching separation in full detail, both the temporal and the spatial aspects of this process were investigated. Apart from the final number and size of the satellite droplets formed, the time it takes and the spatial extension of the structures formed are both of great importance, e.g., for numerical simulations of dense spray flows. In the past this aspect has never been accounted for, nor was it investigated in detail. In the present section we discuss experimental results, first on the temporal then on the spatial scales of the processes and structures of stretching separation.

Figure 14 illustrates the effect of the nondimensional impact parameter X on the nondimensional time $t_f U_0/D_0$ it takes the filament to pinch off the boundary drops. This time is measured from the instant of first contact between the impacting drops. In the figure, curves for the Weber numbers 131, 166, and 220 are depicted. The time to filament pinch-off for a given nondimensional impact parameter X increases monotonically with the Weber number. For all Weber numbers investigated, the nondimensional time decreases with increasing nondimensional impact parameter X. For a range of intermediate values of X between 0.37 and about 0.6, the time to filament pinch-off remains fairly constant, and for larger X the time $t_f U_0/D_0$ continues to decrease even more

steeply than at smaller X. From the measurements of the nondimensional filament pinch-off time, a linear relationship between $t_f U_0/D_0$ and the impact Weber number was found. This relationship is depicted in Fig. 15. The dimensional times t_f vary between 70 and 140 μs. The decrease of t_f with increasing X is reasonable since the filament formation takes longer for more intense contact between the drops, i.e., for larger portions of the drop masses involved in the interaction. The different rates of decrease of t_f with increasing X have to do with the lengths of the filaments which will be discussed with the data of Fig. 17.

In Fig. 16 the nondimensional time $t_{1s} U_0/D_0$ required for the formation of one single satellite droplet is depicted as a function of the nondimensional impact parameter. The four Weber numbers 101, 119, 166, and 220 were investigated. The time is measured between the instant of first contact between the colliding drops and the end of the satellite formation process. It is seen that, for all Weber numbers, the nondimensional time $t_{1s} U_0/D_0$ increases with increasing X at small values of X. For small Weber numbers (e.g., We
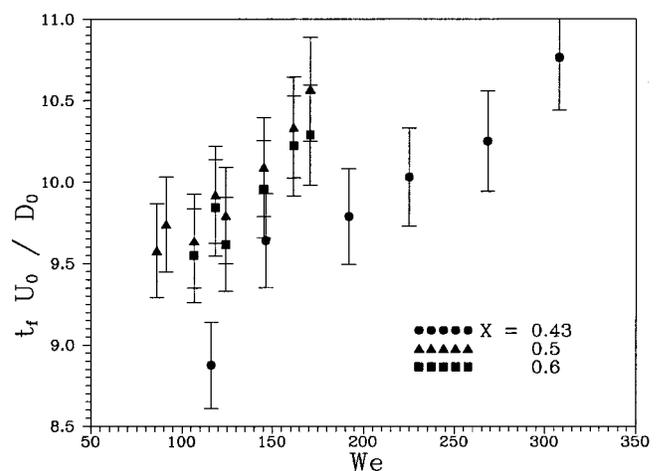

FIG. 15. The nondimensional time to filament pinch-off from the boundary drops as a function of the Weber number for different impact parameters (error 3%).

Phys. Fluids, Vol. 13, No. 9, September 2001

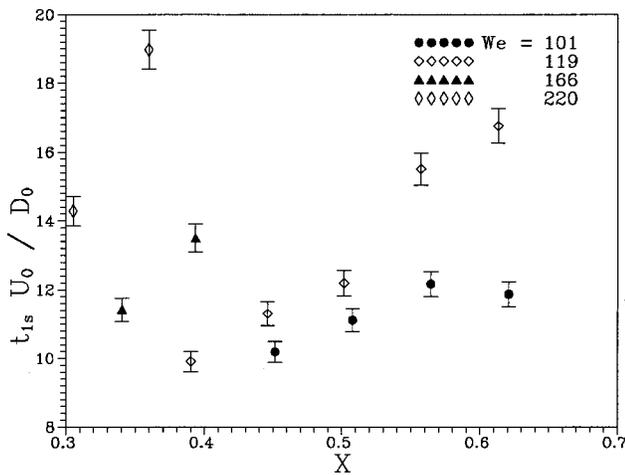Satellite droplets from drop collisions   2475

FIG. 16. The nondimensional time for the formation of one satellite droplet as a function of the nondimensional impact parameter for different Weber numbers (error 3%).

FIG. 18. The nondimensional size of the single satellite droplet as a function of the impact Weber number for three different impact parameters (error 2.4%).

$=101$) we observe a decrease of the time for large impact parameters greater than 0.56. This is a reasonable result, since the relaxation of the longer threads corresponding to larger X around the maximum of the filament length in Fig. 17, takes more time than for shorter filaments. The time t_{1s} for a given impact parameter increases with increasing Weber number. Dimensional times t_{1s} range between 150 and 200 μs. This means that, on average, the formation of one satellite by relaxation of a liquid filament can take place undisturbed only if collisions between the drops occur at average frequencies less than 5 kHz.

The effect of the nondimensional impact parameter on the length of the filament at the instant of pinch-off from the boundary drops is depicted in Fig. 17. The Weber numbers in these experiments were 119, 166, and 220. The filament length was measured on the video image acquired by means of the CCD camera. Due to the angular momentum of the colliding drops, the arrangement of the drops slowly rotates after the collision. Strictly, the length of the filament is to be measured in the plane of the arrangement, which is slightly

tilted relative to the plane of the video image. In previous investigations it was seen, however, that the tilt angle of the filament relative to the observation plane is small. This influence was therefore neglected in the present measurements. The data show that, for all Weber numbers investigated, the length of the filament first increases with increasing nondimensional impact parameter, reaches a maximum value, and then decreases again. The length of the filament reaches its maximum value where the plateaus of the curves in Fig. 14 are observed. The short filaments at small X are due to intense viscous interaction between the colliding drops, which dissipates kinetic energy, while the short filaments at large X are caused by small liquid portions involved in the interaction. The impact parameter, where the maximum filament length occurs, decreases with the Weber number. The maximum values of the filament length are about 550 μm at the highest investigated Weber number of 220. The mean free path length of the drops in the spray in a direction transverse to the main direction of motion must therefore be of this order to allow for the undisturbed formation of such filaments and their subsequent breakup. This aspect has not been accounted for in numerical simulations of dense sprays to date.

Figure 18 illustrates the nondimensional size of a single satellite droplet as a function of the impact Weber number for three different values of the nondimensional impact parameter X. It is seen that, for all X, the nondimensional size of the satellite droplet exhibits an overall tendency to increase with the Weber number. At small We we observe a minimum of the nondimensional satellite size, while a maximum seems to be reached at large We before the nondimensional satellite size tends to decrease again. Due to the scatter observed in the data, however, which is mainly due to uncertainties in adjusting the impact parameter, these observations are uncertain. For a given Weber number, the size of the satellite droplet clearly increases with the nondimensional impact parameter. This is reasonable, since Fig. 17 indicates an increase of the length (and therefore of the volume) of the filament with X for small values of X below 0.55. The results
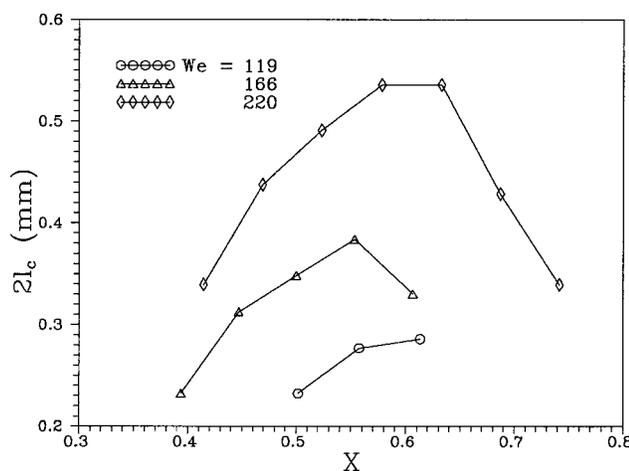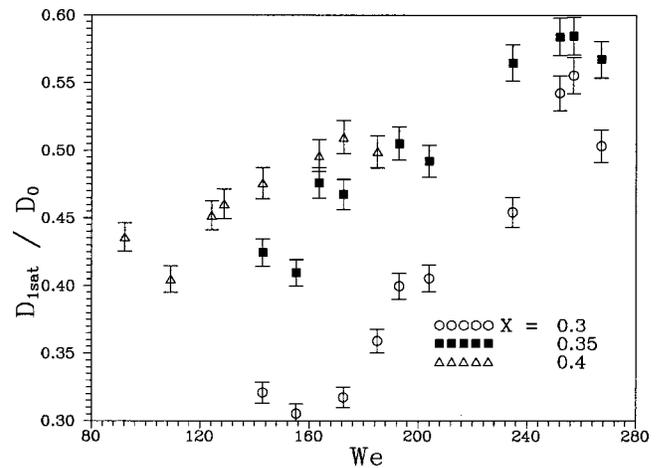

FIG. 17. The length of the filament at the instant of pinch-off from the boundary drops as a function of the nondimensional impact parameter for different Weber numbers.

show that, for a range of small impact parameters investigated, the satellite size may reach half the size of the impacting drops. In order to check the accuracy of the satellite and boundary drop size measurements for some cases, volumes of the drops were compared with those of the impacting drops. For example, for We$=143$ and $X=0.35$, the diameter of the colliding drops was $D_0=89.3$ μm, the diameter of the boundary drops after the collision was 86.7 μm, and the diameter of the satellite droplet was $D_{sat}=37.9$ μm. Calculating the sums of the drop volumes, an error in the volumes of only 5% was found, which indicates good PDA measurements of the drop sizes.

C. Validation of the filament breakup model

In order to validate our filament breakup model presented in Sec. IV, we first consider the case of a head-on collision of two equal drops of water as investigated experimentally by Ashgriz and Poo.[1] In their experiments, the result of head-on and near-head-on collisions of pairs of equal water drops was visualized very nicely; the result of the visualization is depicted in the photographs Figs. 5–7 on plate 1 of that paper. The impact conditions are characterized by the drop size ratio $\Delta=1$ and the nondimensional impact parameters/impact Weber numbers (X/We) of (0.05/23), (0/40), and ($\approx$0/96) in their Figs. 5, 6, and 7, respectively. The numbers of drops formed by these collisions are 2, 3, and 5, respectively. These numbers correspond to our wave numbers $k=\pi/2$, π, and 2π. For the given impact Weber numbers, we find from our model the values of 0.848, 0.709, and 0.58 for the nondimensional filament radius $\tilde{R}_{c,cr}$, which are very accurately confirmed by measurement of the actual values on enlarged copies of the photographs by Ashgriz and Poo,[1] which yield 0.85, 0.72, and 0.6, respectively. For the first case, we see that the pair of values (We/$\tilde{R}_{c,cr}$) $=(23/0.85)$ is located in the stable region of all curves for constant wave number k in Fig. 9, except for $k=\pi/2$. Therefore, for this impact condition, only two drops can be formed after the collision, just as observed in the experiment of Ashgriz and Poo.[1] In the second experiment, depicted in Fig. 6 in Ashgriz and Poo,[1] the point (We/$\tilde{R}_{c,cr}$)$=(40/0.71)$ in Fig. 9 belongs to the unstable regions for the wave numbers $k=\pi/2$ and π. Calculating the nondimensional disturbance energies for the two wave numbers using Eq. (38), we find that the value $\tilde{E}_d=0.0537$ for $k=\pi/2$ and 0.0899 for $k=\pi$. The energy is larger for the larger wave number, so that this disturbance is responsible for the filament breakup and the number of drops formed is 3. The same applies for the third experiment in Fig. 7 of Ashgriz and Poo.[1] The point (We/$\tilde{R}_{c,cr}$)$=(96/0.58)$ in Fig. 9 allows for the conclusion that all four wave numbers $k=\pi/2$, π, $3\pi/2$, and 2π may be responsible for the filament breakup. However, if we again look at the disturbance energies, we find the values $\tilde{E}_d$ $=0.0519$, 0.0828, 0.0196, and 0.0911, respectively, for the four previous wave numbers. The highest energy belongs to $k=2\pi$, so that five drops are formed by the filament breakup after the collision, just as seen on the photographs by Ashgriz and Poo.[1]
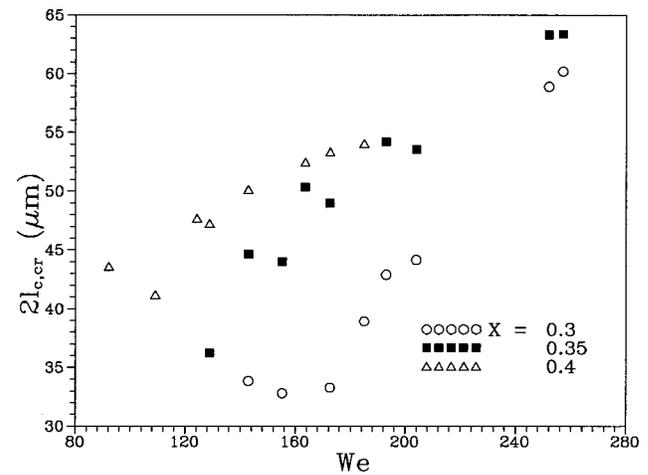

FIG. 19. The length of the filament at pinch-off from the boundary drops for the experimental conditions of Fig. 18. The values compare well with experimental evidence.

Finally we validate the model by looking at our experimental data from cases where a single satellite droplet is formed. For these cases we have measured the sizes of both the boundary drops and the satellite droplet. This enables us to compare the volume of the satellite droplet at the various experimental conditions with the calculated volume of the cylindrical filament formed by pinch-off from the boundary drops. The filament is characterized by its nondimensional length $\tilde{l}_c$ and its nondimensional radius, which is assumed to have the critical value $\tilde{R}_{c,cr}$ for the various cases. Since the state of the filament calculated is critical in the above sense, the nondimensional length is denoted by $\tilde{l}_{c,cr}$, with subscript "cr." The wave number k assumes the value of $\pi/2$ for the formation of a single satellite droplet. Calculating these critical parameters $\tilde{l}_{c,cr}$ and $\tilde{R}_{c,cr}$ from Eqs. (41) and (42) yields the results in Fig. 19. The data clearly exhibit the same behavior with varying Weber number and impact parameter as the nondimensional size of the satellite droplet depicted in Fig. 18. Furthermore, the calculated lengths of the filaments agree well with the visualization results. These are strong indications for realistic predictions from our model.

These examples show that our model is suitable to predict important characteristics of the breakup of a filament produced by unstable binary drop collisions.

VI. SUMMARY AND CONCLUSIONS

In the present article, the stability of binary collisions of propanol-2 drops was studied and the result of unstable collisions quantified. The different structures observed in the experiments depend on the impact Weber number We and the nondimensional impact parameter X. The experiments were carried out using streams of monodisperse drops. The drops interacted pairwise under well-defined impact conditions. The results from the experiments showed that binary collisions of drops with equal diameters leads to a variety of different phenomena occurring after the collisions, which depend on We and X. After the collision, the following different regimes may occur: permanent coalescence; separation after

unstable head-on and near-head-on collisions; formation of one, three, five, or seven satellite droplets by stretching separation. The process of rebound of the impacting droplets was not investigated in the present work.

It was found that the size of the impacting drops influences the processes occurring after the collision. In particular, the maximum observable length of filaments and number of satellite droplets formed by stretching separation may be different for different impacting drop size—even at equal We and X. The boundaries between the regimes with formation of constant numbers of satellite droplets in the stability nomogram are accurately detected in the experiments. The stability limit against stretching separation and the boundary between the regimes, where one and three satellite droplets are formed, coincide even when a given impact Weber number is produced with different pairs of drop size and relative velocity. For the smaller impacting drops, the regimes of three and five satellites start at We=100 and 180, respectively, while for the larger impacting drops they start at We =100 and 150, respectively. The distance between the boundaries of the regimes at high Weber numbers is smaller for the larger impacting drops than for the smaller ones, since the maximum observable number of satellite droplets is higher for larger impacting drop size. Due to the long filaments formed in the case of the large drops from 50 μm orifices, very complicated stretching separation processes were found at Weber numbers greater than 250.

In order to investigate the temporal and spatial characteristics of stretching separation, we measured the time to filament pinch-off from the boundary drops and to formation of a single satellite droplet, and the length of the filament at the instant of pinch-off as functions of the Weber number and the nondimensional impact parameter. We found that

(i)   for all Weber numbers the nondimensional time to filament pinch-off decreases with increasing nondimensional impact parameter;

(ii)   for all impact parameters X the time to filament pinch-off increases with increasing Weber number;

(iii)   for all Weber numbers, the length of the filament increases with increasing X, reaches a maximum value, and thereafter decreases again. For larger Weber numbers, the maximum filament length occurs at larger impact parameters.

For computer simulations of dense sprays, the collisional behavior of the drops in cases where only a single satellite droplet is produced are an important piece of information. Therefore we performed detailed measurements of the time required for the formation of the single satellite droplet and the size of the satellite versus the Weber number for varying impact parameters. We showed that

(i)   for all impact parameters the nondimensional size of the satellite droplet decreases with increasing Weber number, reaches a minimum value, then increases, reaches a maximum value, and finally decreases again; and

(ii)   with increasing nondimensional impact parameter at constant Weber number, the size of the satellite droplet increases.

The theoretical modeling of the collision and breakup process which leads to the satellite droplet formation gave insight into the dependencies of stretching separation on the influencing parameters. Experimental results from Ashgriz and Poo[1] in terms of numbers of droplets formed after head-on and near-head-on collisions of equal-sized water drops are in agreement with the predictions of our model.

ACKNOWLEDGMENTS

[1] N. Ashgriz and J. Y. Poo, "Coalescence and separation in binary collisions of liquid drops," J. Fluid Mech. **221**, 183 (1990).

[2] J. R. Adam, N. R. Lindblad, and C. D. Hendricks, "The collision, coalescence, and disruption of water droplets," J. Appl. Phys. **39**, 5173 (1968).

[3] R. W. Park, "Behaviour of water drops colliding in humid nitrogen," Ph.D. thesis, University of Wisconsin, 1970, p. 577.

[4] P. R. Brazier-Smith, S. G. Jennings, and J. Latham, "The interaction of falling water drops: coalescence," Proc. R. Soc. London, Ser. A **326**, 393 (1972).

[5] V. A. Arkhipov, I. M. Vasenin, and V. F. Trofimov, "Stability of colliding drops of ideal liquid," Zh. Prikl. Mekh. Tekh. Fiz. **3**, 95 (1983).

[6] Y. J. Jiang, A. Umemura, and C. K. Law, "An experimental investigation on the collision behaviour of hydrocarbon droplets," J. Fluid Mech. **234**, 171 (1992).

[7] J. Qian and C. K. Law, "Regimes of coalescence and separation in droplet collision," J. Fluid Mech. **331**, 59 (1997).

[8] J.-P. Estrade, P. Berthoumieu, G. Lavergne, and Y. Biscos, "Experimental investigation of dynamic binary collision of various liquids," in Proceedings of the 8th International Symposium Flow Visualization, Sorrento, Italy (1998).

[9] H. A. Stone, B. J. Bentley, and L. G. Leal, "An experimental study of transient effects in the breakup of viscous drops," J. Fluid Mech. **173**, 131 (1986).

[10] V. Cristini, J. Blawzdziewicz, and M. Loewenberg, "Drop breakup in three-dimensional viscous flows," Phys. Fluids **10**, 1781 (1998).

[11] J. Blawzdziewicz, V. Cristini, M. Loewenberg, and L. Collins, "Sub-Kolmogorov drop breakup in isotropic turbulence," J. Fluid Mech. (in press).

[12] M. Schelkle, A. Karl, and A. Frohn, "The collision of drops: simulation and experiment," Phys. Fluids **8**, S8 (1996).

[13] M. Tjahjadi, H. A. Stone, and J. M. Ottino, "Satellite and subsatellite formation in capillary breakup," J. Fluid Mech. **243**, 297 (1992).

[14] M. P. Brenner, J. R. Lister, and H. A. Stone, "Pinching threads, singularities and the number 0.0304 . . . ," Phys. Fluids **8**, 2827 (1996).

[15] J. Domnick, H. Ertl, and C. Tropea, "Processing of phase/Doppler signals using the cross-spectral density function," Proceedings of the 4th International Symposium on Applied Laser Technology to Fluid Mechanics, paper 3.8, Lisbon, Portugal (1988).

[16] G. Brenn and A. Frohn, "Collision and merging of two equal droplets of propanol," Exp. Fluids **7**, 441 (1989).

[17] G. Brenn, S. Kalenderski, and I. Ivanov, "Investigation of the stochastic collisions of drops produced by Rayleigh breakup of two laminar liquid jets," Phys. Fluids **9**, 349 (1997).